nature communications

Article

https://doi.org/10.1038/s41467-024-55270-2

Mechanistic evaluation of enhanced graphene toxicity to *Bacillus* induced by humic acid adsorption

Received: 27 August 2024

Accepted: 6 December 2024

Published online: 03 January 2025

Check for updates

Xuejiao Zhang[1,2,9], Jin Zeng[2,3,9], Jason C. White[4], Fangbai Li[1], Zhiqiang Xiong[5], Siyu Zhang[1,2], Yuze Xu[1], Jingjing Yang[1], Weihao Tang[1], Qing Zhao[1,6] ✉, Fengchang Wu[7] ✉ & Baoshan Xing[8] ✉

The extensive application of graphene nanosheets (GNSs) has raised concerns over risks to sensitive species in the aquatic environment. The humic acid (HA) corona is traditionally considered to reduce GNSs toxicity. Here, we evaluate the effect of sorbed HA (GNSs-HA) on the toxicity of GNSs to Gram positive *Bacillus tropicus*. Contrary to previous data, GNSs-HA exhibits greater toxicity compared to GNSs. Multi-omics combined with sensitive bioassays and electrochemical methods reveals GNSs disrupt oxidative phosphorylation by causing physical membrane damage. This leads to the accumulation of intracellular reactive oxygen species and inhibition of ATP production, subsequently suppressing synthetic and metabolic processes and ultimately causing bacterial death. Conversely, GNSs-HA directly extracts electrons from bacteria and oxidized biomolecules due to HA-improved electron transfer. This finding suggests that the HA corona does not always mitigate the toxicity of nanoparticles, thereby introducing uncertainty over the interaction between environmental corona and nanoparticles during ecological risk evaluation.

Since its discovery in 2004, graphene nanosheets (GNSs) have been extensively studied for their unique properties that enable multiple applications, including in electronics, catalysis, biomedicine, and environmental fields[1,2]. With increasing production and widespread application of GNSs, there is an increased likelihood of GNSs-based waste entering the aquatic environment, raising concerns over potential environmental damage. Previous studies have shown that GNSs exhibit significant toxicity to aquatic organisms through oxidative stress, physical disruption of cell membranes or cell walls, and electron transfer between biological molecules and GNSs[3,4].

Humic acid (HA) is the main component of natural organic matter (NOM) and is ubiquitous in aqueous systems. When GNSs enter the aquatic environment, formation of a HA corona can be expected, which alters the physicochemical properties of GNSs, subsequently impacting their transport, fate, and toxicity. GNSs can be internalized by algae and accumulate intracellularly, interfering with biological processes[5]. Notably, the interaction between GNSs and bacteria

[1]National-Regional Joint Engineering Research Center for Soil Pollution Control and Remediation in South China, Guangdong Key Laboratory of Integrated Agro-environmental Pollution Control and Management, Institute of Eco-environmental and Soil Sciences, Guangdong Academy of Sciences, Guangzhou 510650, China. [2]Key Laboratory of Pollution Ecology and Environmental Engineering, Institute of Applied Ecology, Chinese Academy of Sciences, Shenyang 110016, China. [3]University of Chinese Academy of Sciences, Beijing 100049, China. [4]The Connecticut Agricultural Experiment Station, New Haven, CT 06504, US. [5]State Key Laboratory of Radiation Medicine and Protection, School of Radiological and Interdisciplinary Sciences (RAD-X), Suzhou Medical College, Soochow University, Suzhou 215123, China. [6]Wuhu Haichuang Environmental Protection Technology Co., Ltd., Wuhu 723309, China. [7]State Key Laboratory of Environmental Criteria and Risk Assessment, Chinese Research Academy of Environmental Sciences, Beijing 100012, China. [8]Stockbridge School of Agriculture, University of Massachusetts, Amherst, MA 01003, USA. [9]These authors contributed equally: Xuejiao Zhang, Jin Zeng. ✉e-mail: zhaoqing@iae.ac.cn; wufengchang@vip.skleg.cn; bx@umass.edu

typically occurs at the nano-bio interface. Previous studies have demonstrated that HA reduces GNSs toxicity to algae, largely by mitigating physical damage through reduced direct contact, leading to significantly less intracellular or extracellular reactive oxygen species (ROS)[4,6]. However, the impact of HA corona on the bacterial toxicity of GNSs is unknown.

Unlike algae, which can internalize GNSs, bacterial interactions with GNSs are largely restricted to the cell membrane. In addition to inducing physical damage to the membrane, GNSs can also cause cell membrane dysfunction through chemical reactions such as electron transfer[7]. Previous studies have shown that GNSs can serve as strong electron acceptors and extract electrons directly from the electron transport chain (ETC) in the cytoplasmic membrane, resulting in compromised membrane integrity and reduced ATP production[7,8]. While the HA corona typically alleviates the physical membrane damage caused by 2D nanomaterials[9], the impact on chemical interactions between GNSs and the bacterial membrane is unclear.

The electron extraction capacity from the ETC is influenced by the electrical conductivity or band structure of the material in question. Yeung et al. reported that manipulating the electrical conductivity of vanadium dioxide by tungsten doping enhanced antimicrobial activity by facilitating electron extraction from the bacterial respiratory chain.

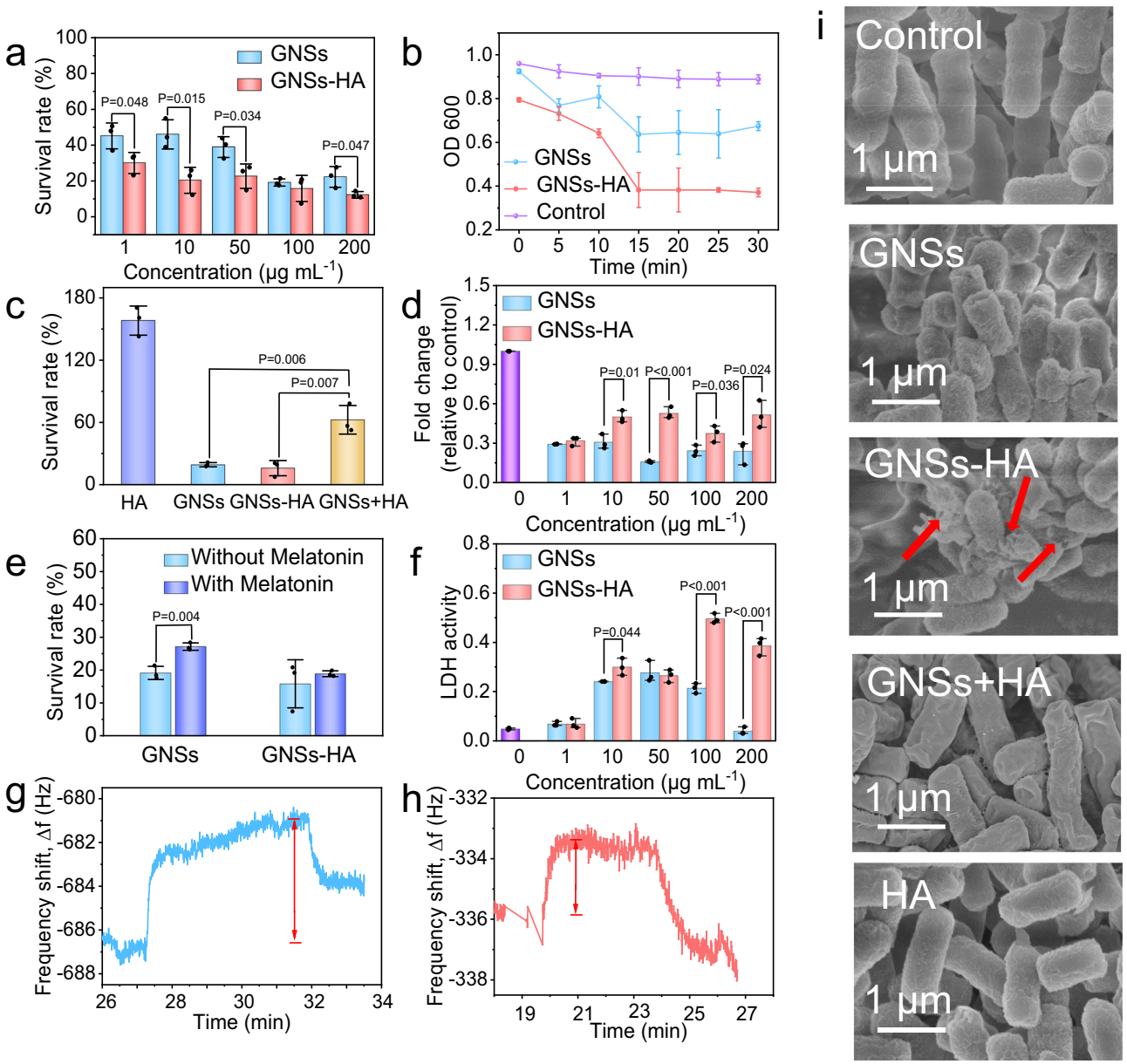

Fig. 1 | Toxicity, oxidative stress, and membrane damage of bacteria. a Survival rate of *B. tropicus* after treatment with different concentrations of GNSs and GNSs-HA for 12 h; **b** Effects of GNSs and GNSs-HA on the OD value of *B. tropicus* within 30 min at the concentration of 100 μg mL^{-1}; **c** Survival rate of *B. tropicus* after treatment with HA at 1.4 μg mL^{-1} and GNSs, GNSs-HA, and GNSs+HA at the concentration of 100 μg mL^{-1} for 12 h; **d** GSH/GSSG ratio in *B. tropicus* after treatment with GNSs and GNSs-HA for 12 h as compared to the value without any treatment; (**e**) Survival rate of *B. tropicus* after treatment with 100 μg mL^{-1} of GNSs and GNSs-HA for 12 h in the presence and absence of melatonin; **f** LDH activity of *B. tropicus* after treatment with different concentrations of GNSs and GNSs-HA; Frequency variations of the DOPC vesicles after introducing 100 μg mL^{-1} of GNSs (**g**) and GNSs-HA (**h**); (**i**) Morphology of *B. tropicus* without any treatment or after treatment with 100 μg mL^{-1} of GNSs, GNSs-HA, and GNSs+HA, and 1.4 μg mL^{-1} of HA for 12 h. For (**a**–**f**) data are shown as mean ± SD ($n = 3$). Each data point represents a biologically independent replicate. *P* values were determined by two-sided *T*-test.

This process induced oxidative stress, disrupted synthesis and metabolism, and ultimately led to membrane perturbation and leakage of intracellular matter[10]. Importantly, HA can modify the band structure of semiconductive materials through physical adsorption[3,11]. GNSs are semimetal materials with a zero bandgap that can be modified by noncovalent functionalization through surface transfer doping[12]. Based on this information, we hypothesize that HA can alter the band structure of GNSs and influence electron transfer between GNSs and bacteria.

In the current study, we evaluated the effect of HA adsorption on the bacterial toxicity of GNSs by exposing GNSs and HA-sorbed GNSs (GNSs-HA) to Gram positive *Bacillus tropicus* (*B. tropicus*). Measured end points included intracellular ROS, GSH oxidation, bacterial morphology, LDH release, model membrane integrity, oxidative phosphorylation, ATP synthesis, electron transfer, and biomolecule oxidation. In addition, multi-omic techniques were used to investigate the mechanism of HA-enhanced GNSs toxicity to *B. tropicus*. The universality of the toxicity trend was evaluated on other strains, including Gram-negative *Escherichia coli* k12 (*E. coli* k12), Gram-positive *staphylococcus aureus* (*S. aureus*) and *Bacillus subtilis* (*B. subtillis*). This study highlights the importance of considering the interaction between engineered nanoscale pollutants (ENPs) and electroactive NOM during ecological risk evaluation.

Results

Characterizations of GNSs and GNSs-HA

Chemical adsorption was found to play a dominant role in the formation of GNSs-HA via adsorption kinetics investigation, suggesting the involvement of electron sharing or electron transfer between HA and GNSs (Supplementary Fig. 1). After HA adsorption, the smooth lamellar structure of GNSs became rough and uneven (Supplementary Figs. 2 and 3), with the average lateral size decreasing from 236.9 ± 50.2 to 169.0 ± 64.0 nm, and the average thickness increasing from 1.1 ± 0.3 to 1.7 ± 0.7 nm (Supplementary Fig. 4). The interactions between GNSs and HA were further explored by Fourier transform infrared spectroscopy (FTIR), X-ray photoelectron spectroscopy (XPS), and Raman spectroscopy. Compared to the bare GNSs, newly emerged peaks located at 3689, 3646, and 2651 cm^{-1} were observed in the FTIR spectrum of GNSs-HA, due to the stretching vibrations of -OH and -COOH groups in HA (Supplementary Fig. 5)[13,14]. In the XPS spectrum of GNSs, there were three peaks at 284.6, 285.4, and 288.4 eV (Supplementary Fig. 6a), assigned to C-C, C-OH, and O-C = O groups, respectively[15], indicating that GNSs were slightly oxidized. In contrast, the intensity of C-OH and O-C = O peaks were much stronger and a new peak at 286.6 eV (assigned to C-O) appeared after HA adsorption (Supplementary Fig. 6b).

Raman spectroscopy further isolated changes of the layered structure of GNSs with HA hybridization. Two prominent peaks located at ~1580 and ~1313 cm^{-1} were observed in the Raman spectrum of GNSs (Supplementary Fig. 7), corresponding to the sp^2 (G) and sp^3 (D) hybridized carbon atoms of GNSs, respectively. The I_D/I_G ratio, representing the structural change of GNSs, decreased from 0.95 to 0.82 after HA adsorption, indicating the disorder degree of GNSs decreased and the crystalline degree increased, thereby improving conductivity[6]. Moreover, the decreased I_D/I_G ratio also indicates the existence of the π-π interaction between GNSs and HA, which promotes electronic shuttling between the two analytes[16].

Effects of HA on the bacterial toxicity of GNSs

As the concentration of GNSs increased from 1 to 200 μg mL^{-1}, the survival rate of *B. tropicus* decreased from 45% to 19.23%. Surprisingly, HA adsorption caused a significant increase in GNSs toxicity. While the disparity at 100 μg mL^{-1} was not statistically significant, GNSs-HA exhibited a 2.62% greater inhibitory effect. The survival rate of *B. tropicus* after GNSs-HA treatment decreased from 30.33% to 15.8% at 1 to 100 μg mL^{-1} (Fig. 1a). However, the toxicity did not further increase at 200 μg mL^{-1} due to the obvious precipitation of GNSs and GNSs-HA (Supplementary Fig. 8). The short-term growth curve exhibited that the inhibitory effect of both GNSs and GNSs-HA was largely complete within 30 min, with a greater effect for GNSs-HA (Fig. 1b). When treated with HA, the survival rate of *B. tropicus* was 1.58 times higher than the control (Fig. 1c), excluding the contribution of HA on the stronger bacterial toxicity of GNSs-HA. These findings contradict the traditional understanding that HA alleviates the toxicity of 2D nanomaterials to algae and other species as reported in the literature[3,4,6,17–19].

Given that NOM in the surface-bound and dissolved states may differentially impact nanotoxicity[18], we investigated the survival rate of *B. tropicus* treated with GNSs in the presence of dissolved HA (GNSs +HA). Interestingly, unlike surface-bound HA, which either aggravated or maintain the toxicity, dissolved HA significantly improved bacterial survival compared to the GNSs group (Fig. 1c). Therefore, our results demonstrated that HA in the surface-bound state was responsible for the observed enhanced GNSs toxicity to *B. tropicus*.

Oxidative stress

Neither GNSs nor GNSs-HA increased the ROS level in *B. tropicus* after 2 h exposure, although GNSs induced a concentration-dependent increase after 12 h (Supplementary Fig. 9). These results suggest that ROS-dependent oxidative stress was not the promoter of GNSs- or GNSs-HA-induced bacterial toxicity. More specifically, within the first 2 h, the antioxidative system of *B. tropicus* was capable of alleviating excess ROS produced intracellularly. However, the antioxidative system became overwhelmed after 12 h of exposure to GNSs, leading to the accumulation of ROS and subsequent bacterial toxicity[20].

Glutathione (GSH) is an antioxidant to protect cellular components from oxidative stress-induced damage[21]. In the presence of free radicals, GSH can generate glutathione disulfide (GSSG), which can react with sulfhydryl (-SH) containing biomolecules, leading to toxic effects[22]. In our study, the GSH/GSSG ratio in the experimental groups decreased, and this decrease was more pronounced with GNSs (Fig. 1d). However, the oxidation of GSH to GSSG should have been suppressed with GNSs due to the down-regulation of GSH oxidation-related proteins (Supplementary Fig. 10), indicating that the significant oxidation of GSH is likely a result of greater ROS. In contrast, GNSs-HA might have induced GSH oxidation through a non-ROS-dependent pathway. In the presence of antioxidant melatonin, the survival rate of *B. tropicus* was slightly increased from 19.13% to 27.11% with GNSs but was unchanged with GNSs-HA (Fig. 1e). These results suggest that ROS played a minor role in the toxicity of GNSs and was not involved in GNSs-HA-induced bacterial toxicity.

Membrane damage

In addition to oxidative stress, membrane damage also plays a significant role in the antibacterial behavior of 2D nanomaterials due to the nanoknife effect[23]. Both GNSs and GNSs-HA caused significant membrane damage to *B. tropicus* (Fig. 1f, i, and Supplementary Fig. 11). Although sharp edges of the GNSs lamellar structure were passivated by HA (Supplementary Fig. 2), which was expected to alleviate direct physical damage[4], GNSs-HA induced greater membrane damage than did GNSs, with distorted and shriveled patterns evident by SEM. Consistent with SEM observations, greater LDH release and more significant alterations in the expression of membrane integrity-related proteins were observed after GNSs-HA but not GNSs treatments (Supplementary Fig. 12 and 13), indicating more extensive membrane damage. In contrast, HA did not cause any observable damage to the bacterial membrane. Moreover, GNSs+HA resulted in less pronounced membrane damage than GNSs and GNSs-HA (Fig. 1i and Supplementary Fig. 11), demonstrating the protective effect of HA in its dissolved state.

Cell membrane can be disrupted by 2D nanomaterials either through physical damage or by chemical reactions[24–26]. The physical membrane damage was monitored by quartz crystal microbalance

https://doi.org/10.1038/s41467-024-55270-2

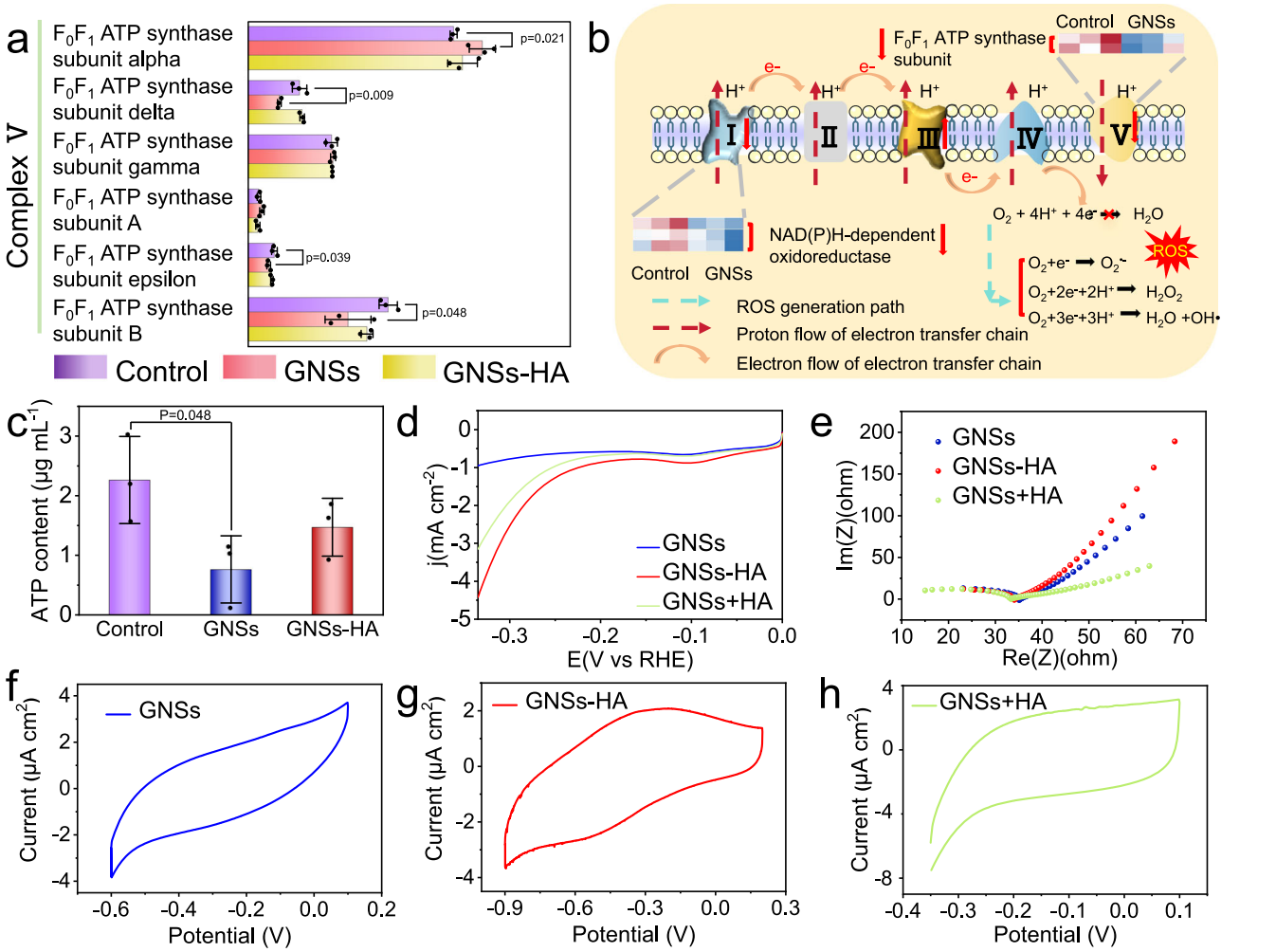

Fig. 2 | Bacterial respiratory chain and electrochemical tests. a Changes in ATP synthase-related proteins after GNSs or GNSs-HA treatments at the concentration of 100 μg mL^{-1} for 60 min; **b** Schematic diagram of respiratory chain changes in the GNSs treatment group; **c** ATP content after treatment with GNSs and GNSs-HA at the concentration of 100 μg mL^{-1} for 60 min. Electron transfer between *B. tropicus* and GNSs or GNSs-HA represented by LSV curves (**d**), Nyquist plots (**e**), and CV curves (**f**–**h**). In the electrochemical tests, both GNSs and GNSs-HA were coated onto carbon fiber paper at a density of 0.5 mg cm^{-2}. For the GNSs+HA group, GNSs at a loading of 0.5 mg cm^{-2} were applied to the carbon fiber paper, and HA was introduced into the bacterial suspension at a concentration of 1.4 μg mL^{-1}. The electrochemical tests were performed at least in triplicate with similar results. For (**a**, **c**) data are shown as mean ± SD ($n = 3$). Each data point represents a biologically independent replicate. *P* values were determined by two-sided *T*-test.

with dissipation (QCMD). GNSs elicited a more obvious frequency increase (5.86 Hz) compared to GNSs-HA (2.53 Hz) (Fig. 1g, h, and Supplementary Fig. 14), demonstrating greater physical damage to the membrane. S-layer proteins (SLPs) are cell wall-related proteins located on the outermost layer of microorganisms that are in direct contact with the external environment and protect bacterial cells against xenobiotics[27]. The proteomics data showed that the SLPs of *B. tropicus* decreased more significantly with GNSs than GNSs-HA (Supplementary Fig. 15), suggesting that HA adsorption reduced the physical interaction-driven membrane damage of GNSs. Therefore, it is clear that chemical oxidation dominates the membrane damage caused by GNSs-HA.

Disturbance of oxidative phosphorylation

As most electron transfer-related proteins are located on the plasma membrane[28], the membrane integrity is closely related to respiratory ETC function. The ETC consists of several protein complexes, including complex I (NADH-ubiquinone oxidoreductase), complex II (succinate dehydrogenase), complex III (ubiquinol-cytochrome c reductase), and complex IV (cytochrome oxidase complex). The ETC combines with complex V (ATP synthase) to constitute the oxidative phosphorylation system, which plays a crucial role in generating ATP to sustain cellular activity[29–31].

Multi-omics analyses were used to investigate the effect of GNSs, GNSs-HA, GNSs+HA, and HA on the oxidative phosphorylation system (Fig. 2a, Supplementary Figs. 16 and 17). In complex I, NAD(P)H-dependent oxidoreductases (WP_000683422.1, WP_025991632.1), were down-regulated in the GNSs group compared to the control. In complex II, succinate dehydrogenase flavoprotein subunit was up-regulated with GNSs, while succinate dehydrogenase cytochrome B558 was down-regulated with GNSs-HA. Menaquinol-cytochrome c reductase cytochrome b/c subunit, a main component of complex III, was up-regulated with GNSs exposure. Obvious changes in complex IV were observed with both GNSs and GNSs-HA. GNSs down-regulated aa3 quinol oxidase subunit I and up-regulated cytochrome c-550 and cytochrome c oxidase subunit III, while GNSs-HA down-regulated aa3 quinol oxidase subunit I, cytochrome aa3 quinol oxidase subunit III, and cytochrome c-551. With GNSs, complex V, such as F0F1 ATP synthase subunit alpha, was significantly up-regulated, and the F0F1 ATP synthase subunit delta, F0F1 ATP synthase subunit epsilon, and F0F1

ATP synthase subunit B were significantly down-regulated; importantly, there were no such changes with GNSs-HA (Fig. 2a). However, the transcriptomic data showed that the expression of genes related to complex I, including *nuo L*, *nuo K*, *nuo J*, *nuo H*, *nuo D*, and *nuo C*, were significantly up-regulated under GNSs exposure (Supplementary Fig. 18). The *nuo* genes encode the subunits of complex I and are responsible either for the assembly or the stability of the bacterial complex I. *Nuo C* and *nuo D* constitute the connecting fragment, while *nuo H*, *nuo J*, *nuo K*, *nuo L* constitute the membrane fragment[32]. The up-regulation of these *nuo* genes may be due to a stress response at the transcriptional level as a function of decreased complex I.

These disruptions were primarily manifested through significant down-regulation of complex I and V, up-regulation of complex III, and interference with complex II and IV upon GNSs exposure (Fig. 2b). Complex I (NADH-ubiquinone oxidoreductase) passes electrons from NADH to ubiquinone through a series of enzyme-bound redox centers, which then serves as the primary entry point for electrons into the ETC[33]. The down-regulation of complex I subunits could induce the ETC dysfunction, leading to the generation of excess ROS[34], which supports our findings that ROS accumulates with GNSs treatment. Complex V (ATP synthase) is responsible for ATP synthesis via the proton gradient generated by ETC[35]; down-regulation of ATP synthase may lead to the decrease of ATP levels[36]. This impact on oxidative phosphorylation by GNSs was likely due to a disruption of electron transfer between iron-sulfur centers, as indicated in a previous study[8]. Conversely, GNSs-HA disruption was less severe and primarily affected complex II and IV.

In contrast, HA induced a negligible effect on the oxidative phosphorylation system, except for the up-regulation of menaquinol-cytochrome c reductase cytochrome b subunit in complex III. Moreover, GNSs+HA had a minor influence on the oxidative phosphorylation system, with the up-regulation of menaquinol-cytochrome c reductase cytochrome b subunit in complex III and the down-regulation of cytochrome c oxidase subunit III in complex IV (Supplementary Fig. 17), which was in sharp contrast to the effects of GNSs. These findings indicate that both surface-bound and dissolved HA could mitigate the disturbance of oxidative phosphorylation system induced by GNSs.

ATP synthesis

Disturbance of oxidative phosphorylation by GNSs inhibited ATP synthesis, reducing ATP content compared to the control (Fig. 2c). Conversely, there was no significant change in ATP content with GNSs-HA. Since sufficient energy supply is required to maintain physiological function, ATP deficiency could impair bacterial synthesis and metabolism. Five differentially abundant proteins (DAPs) associated with synthesis- and metabolism-related pathways were significantly down-regulated with GNSs, while one was up-regulated with GNSs-HA (Supplementary Figs. 19 and 20), indicating the inhibitory effect of GNSs on *B. tropicus* synthesis and metabolism. Since synthetic and metabolic processes require ATP and are necessary for bacterial growth and reproduction[37–39], the deficiency of ATP induced by GNSs inhibited synthesis and metabolism and ultimately led to a reduction in bacterial growth.

Complex V (ATP synthase) is composed of F_0 and F_1 units, which act as the proton channel and catalyst for ATP synthesis, respectively[30]. The synthesis of each ATP molecule requires 2 ~ 3 protons to be transported across the membrane from the intermembrane space to the cytoplasm by the proton channel[40]. The down-regulation of complex V in the GNSs group interfered with proton pump function, inhibiting the delivery of protons into the cytoplasm (Fig. 2a, b). As the terminal electron acceptor of aerobic bacteria, intracellular O_2 is reduced to H_2O at the terminal of the ETC (Eq. 1). With insufficient proton pumping in the cells, incomplete reduction of O_2 occurred (Eqs. 2–4), resulting in the accumulation of intracellular ROS[41]. This likely explains the delayed elevation of intracellular ROS with GNSs (Supplementary Fig. 9). Conversely, GNSs-HA did not interfere with the expression of complex V (Fig. 2a), which allows the occurrence of four-electron reduction of O_2 to water (Eq. 1), thus avoiding the generation of ROS.

$$\frac{1}{2}O_2 + 2H^+ + 2e^- \rightarrow H_2O \quad (1)$$

$$O_2 + e^- \rightarrow O_2^{\bullet -} \quad (2)$$

$$O_2 + 2e^- + 2H^+ \rightarrow H_2O_2 \quad (3)$$

$$O_2 + 3e^- + 3H^+ \rightarrow H_2O + OH\bullet \quad (4)$$

Electron transfer between *B. tropicus* and graphenes

Although it is still unclear why GNSs-HA elicited higher toxicity than GNSs, more significant membrane damage with GNSs-HA from chemical oxidation, as opposed to physical disruption, provides a valuable clue. If an oxidation reaction occurs between *B. tropicus* and GNSs or GNSs-HA, electron transfer is inevitable and this can be characterized by an electrochemical method[42–44]. The linear sweep voltammetry (LSV) curves, Nyquist plots, and cyclic voltammetry (CV) curves demonstrated the electron transfer between *B. tropicus* and substances followed the sequence of GNSs-HA > GNSs+HA > GNSs (Fig. 2d–h). The phenomenon of HA-enhanced electron transfer has been previously observed in microbial fuel cells[45]. Notably, the surface-bound HA made a greater impact on the electron transfer efficiency than the dissolved HA.

Kelvin probe force microscopy (KPFM) was performed to determine the electron flow direction by measuring the alteration of bacterial surface potential before and after treatments. Compared to the control, the surface potential of *B. tropicus* was enhanced by 161 and 208 mV in the presence of both GNSs and GNSs-HA (Fig. 3a–c), but was decreased by 27 and 59 after exposure to GNSs+HA and HA (Supplementary Fig. 21). These results imply that, unlike GNSs and GNSs-HA which act as electron acceptors, HA and GNSs+HA appeared to donate electrons to *B. tropicus*. This electron donation helps to prevent the loss of biological electrons and protect biomolecules from oxidation. According to the proteomic data, electron transfer flavoprotein subunits were up-regulated in GNSs-treated cells (Supplementary Fig. 22), indicating more endogenous electrons were delivered via extracellular electron transfer (EET). However, more biological electrons were lost in GNSs-HA-treated cells (Fig. 3c). In addition, GNSs and GNSs-HA may further transfer the obtained electrons to extracellular O_2; the oxygen consumption rate was in the order of GNSs-HA>GNSs >control (Fig. 3d). Since no extracellular ROS was detected (Fig. 3e), the four-electron reduction of O_2 to water likely occurred (Eq. 1), indicating the oxidation of bacterial components was not derived from extracellular ROS. Consequently, there should be other pathways, including direct oxidation of biological components, contributing to the loss of electrons from GNSs-HA-treated *B. tropicus*, as facilitated by HA-enhanced electron transfer.

Oxidation of bacterial components

As a result of the loss of biological electrons, biomolecules such as lipid membrane components and intracellular macromolecules can be oxidized. After treatment with GNSs, lipid peroxidation as measured by malondialdehyde (MDA) followed a dose-dependent pattern (Fig. 3f), which was proportional to the intracellular ROS level, suggesting excessive ROS might explain GNSs-induced lipid peroxidation. Surprisingly, GNSs-HA induced even stronger lipid peroxidation, despite not leading to an increase in the intracellular or extracellular

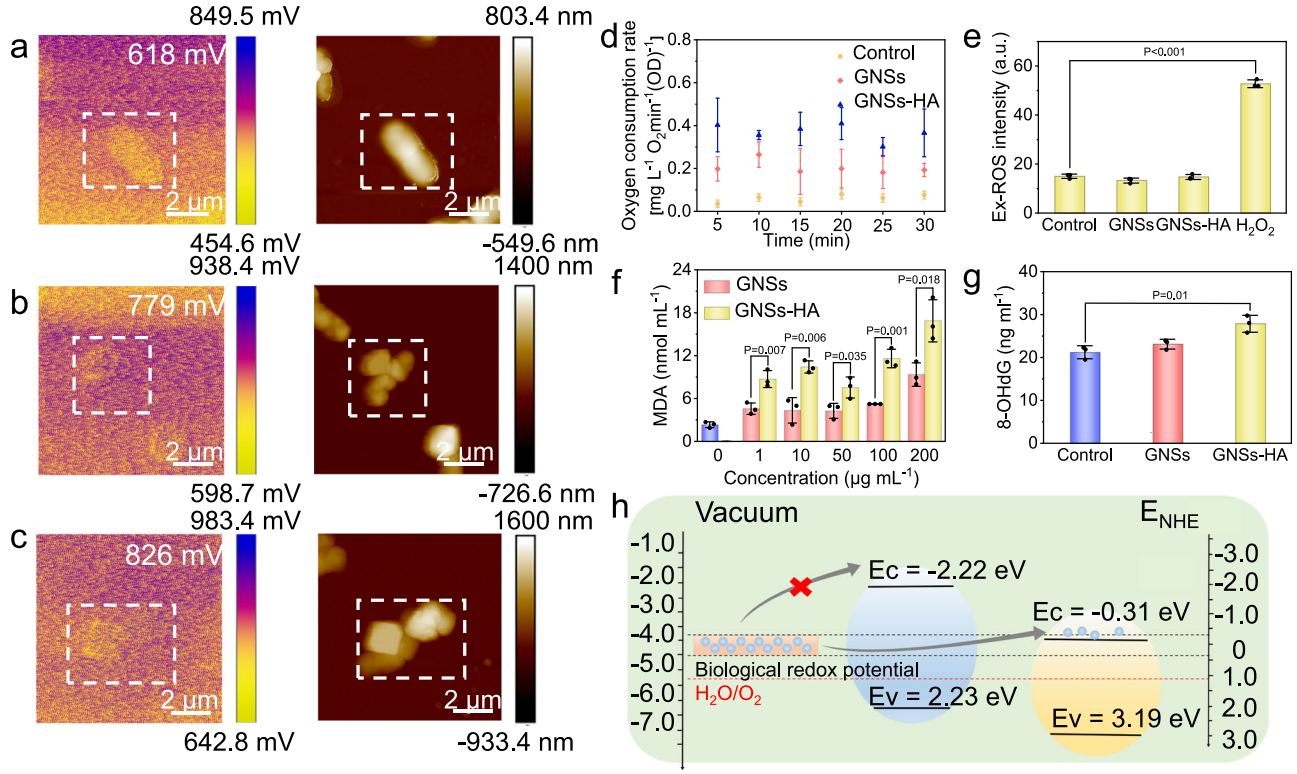

Fig. 3 | Electron-transfer-mediated biomolecule oxidation mechanism. KPFM images of *B. tropicus* without any treatment (**a**), or treated with GNSs (**b**) and GNSs-HA (**c**) at the concentration of 100 μg mL^{-1} for 60 min, the surface potential values exhibit in the top right corner of the left-hand images. All experiments were performed at least in triplicate with similar results; (**d**) Oxygen consumption rate of *B. tropicus* treated with GNSs and GNSs-HA at the concentration of 100 μg mL^{-1} within 30 min. **e** Extracellular ROS level in the bacterial culture medium after treatment with GNSs (100 μg mL^{-1}), GNSs-HA (100 μg mL^{-1}), and H_2O_2 (1%) for 12 h. MDA (**f**) and 8-OHdG content (**g**) in *B. tropicus* after exposure to GNSs and GNSs-HA at the concentration of 100 μg mL^{-1} for 12 h. **h** Schematic illustration of the possible electron transfer pathway between *B. tropicus* and the materials. For (**d**–**g**) data are shown as mean ± SD ($n = 3$). Each data point represents a biologically independent replicate. *P* values were determined by two-sided *T*-test.

ROS (Supplementary Fig. 9, Fig. 3e). Given this, direct oxidation by GNSs-HA through electron transfer could be a plausible mechanism[21,43]. Importantly, only GNSs-HA oxidized intracellular DNA, as determined by the level of 8-hydroxy-deoxyguanosine (8-OHdG), which is a marker of DNA oxidative damage (Fig. 3g)[23]. Several purine metabolism-related genes were significantly altered under GNSs-HA stress (Supplementary Fig. 23), suggesting the disturbance of purine metabolism, which might be due to oxidative damage of guanine in DNA driven by electron transfer rather than ROS.

Discussion

HA is commonly known as a detoxifying agent for nanoparticles. Contrary to this common viewpoint, our study demonstrated that surface-bound HA enhanced the toxicity of GNSs to Gram-positive *B. tropicus* (Fig. 4). Through a detailed mechanistic analysis conducted at concentrations of 50 and 100 μg mL^{-1} (Supplementary Fig. 24–29), we discovered that the primary toxicological pathways of GNSs differ when combined with HA.

Specifically, GNSs caused serious physical membrane damage, leading to the disturbance of oxidative phosphorylation that not only induced intracellular ROS accumulation but also inhibited ATP synthesis. This disruption subsequently led to energy deficiency, which inhibited synthesis and metabolism and caused cell death. Conversely, GNSs-HA induced less physical membrane damage but elicited greater LDH leakage and lipid peroxidation. Additionally, despite the lack of intracellular or extracellular ROS, we observed the oxidation of GSH and DNA, indicating that GNSs-HA directly extracted electrons from *B. tropicus* and oxidized biomolecules. While both materials can serve as electron acceptors through EET, electron transfer from *B. tropicus* to GNSs-HA was more efficient than GNSs (Fig. 2d–h). The conduction band (E_c) of semiconductor overlapping with the biological redox potential (BRP, −4.12 ~ −4.84 eV) allows for electron transfer from biological couples to the E_c, leading to the oxidation of biological substances[46,47]. The E_c of GNSs-HA (Fig. 3h, Supplementary Fig. 30) was within the scope of BRP, enabling spontaneous electron transfer from *B. tropicus* biomolecules to GNSs-HA. Therefore, the enhanced toxicity of GNSs-HA to *B. tropicus* is primarily attributed to electron-transfer-mediated biomolecule oxidation, a mechanism unique to GNSs-HA. It is noteworthy that this electron-transfer-mediated biomolecule oxidation mechanism persists even at a concentration where there is no significant difference in toxicity (100 μg mL^{-1}). This finding underscores that the manifestation of this mechanism in *B. tropicus* for GNSs-HA is not dependent on concentration, as long as there is sufficient physical membrane damage.

Additionally, both GNSs and GNSs-HA may hinder nutrient absorption by wrapping *B. tropicus*, indicating that their toxicological impacts result from multiple interactive mechanisms rather than a single cause. The proportion of GNSs and GNSs-HA in dispersed versus agglomerated states fluctuates with varying exposure dosages. The dispersion of these nanosheets correlates significantly with the extent of physical membrane damage, which is either the primary toxicological pathway for GNSs or a necessary precondition for the electron-transfer-mediated oxidation of biomolecules by GNSs-HA. In contrast, the agglomeration of these nanosheets is related to a nutrient deficiency, in particular at elevated concentrations. Consequently, the concentration of GNSs and GNSs-HA in the experimental setup

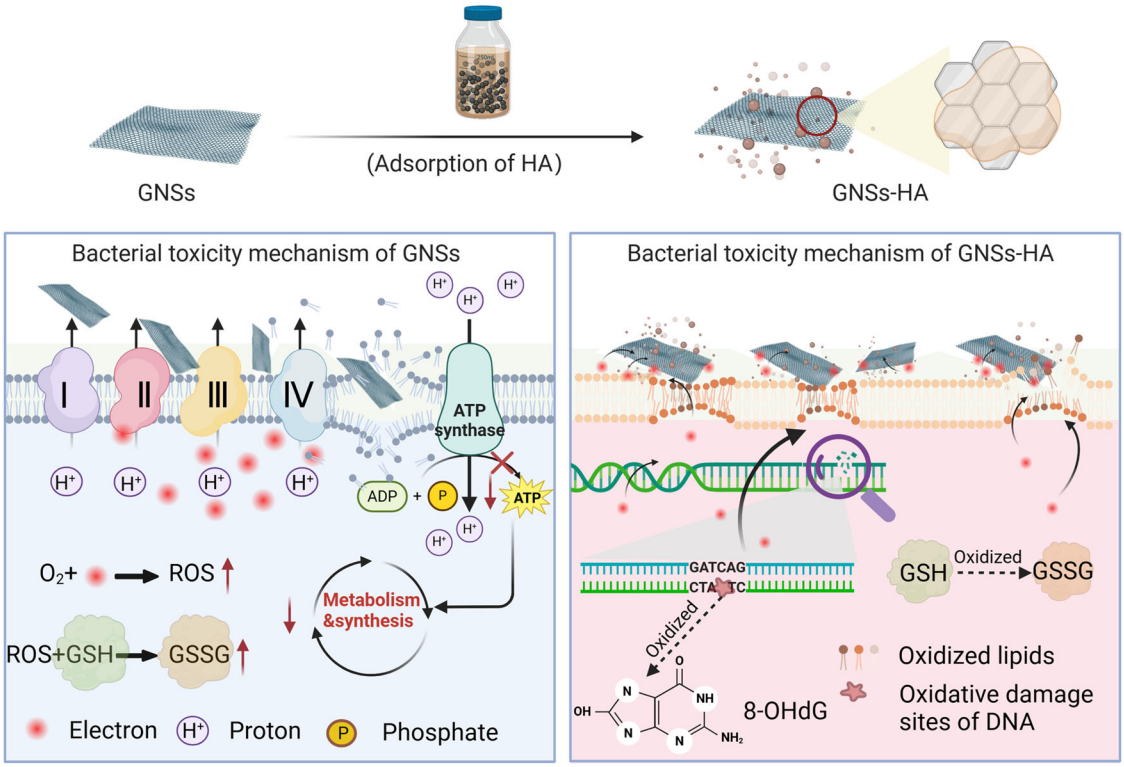

Fig. 4 | Schematic illustration of different mechanisms of bacterial toxicity from GNSs or GNSs-HA exposure. GNSs induced physical damage to the cell membrane, which disrupted oxidative phosphorylation, leading to ROS accumulation and energy deficiency; GNSs-HA directly extracted electrons from *B. tropicus* across the mildly destroyed membrane, leading to the oxidation of biomolecules. Created in BioRender. Jin, Z. (2023) https://BioRender.com/f32z797.

influences their interactions with *B. tropicus* by altering the equilibrium between dispersed and agglomerated forms, thereby determining the contribution of each toxicological mechanism.

Toxicity evaluations were also conducted on Gram-negative *E. coli* k12, Gram-positive *S. aureus*, and *B. subtillis* to assess the universality of HA-enhanced toxicity. Consistent with the findings in *B. tropicus*, *B. subtillis* was also found to be more susceptible to GNSs-HA, while the toxicity of GNSs to *E. coli* k12 and *S. aureus* was reduced after HA adsorption (Supplementary Fig. 31). The distinct toxicological responses may be attributed to the differences in bacterial membrane structure and morphology, which affect the interactions of GNSs and GNSs-HA with bacterial cells[48–52]. Specifically, the outer membrane of Gram-negative *E. coli* acts as a barrier against the physical damage from the sharp edges of GNSs[53]. Additionally, the cell membrane's high resistance, with the conductivity of 10^{-7} S m^{-1} [54], limits electron outflow from the conductive interior of *E. coli* to GNSs-HA, despite the overlap of E_c with BRP. In contrast, rod-shaped Gram-positive bacteria such as *B. tropicus* and *B. subtillis* are more vulnerable to physical membrane damage from GNSs-HA, which, although less than that caused by GNSs alone, is pivotal for increased electron loss and subsequent oxidation of biological substances. Consequently, the electron-transfer-mediated biomolecule oxidation mechanism necessitates both a certain extent of physical membrane damage and overlapping of the GNSs-HA's conduction band with the biological redox potential.

Conversely, despite lacking an outer membrane, the smaller, spherical shape of *S. aureus* allows these bacterial to use GNSs and GNSs-HA as shelters, limiting the exposure of their membranes to the lamellar edges compared to rod-shaped cells[55]. While the cutting effect of GNSs and GNSs-HA is less pronounced in *S. aureus* due to the presence of fewer sharp edges, the smaller size of the sheet-like structures enables them to envelop *S. aureus* more effectively, hindering nutrient uptake and ultimately leading to bacterial death. Therefore, the contribution of each mechanism to overall toxicity depends on both the exposure concentration and the bacterial strain.

In the current work, we reported that the toxicity of GNSs-HA to *B. tropicus* was higher than that of bare GNSs across the experimental concentrations, contradicting the widely held belief that HA mitigates the toxicity of ENPs. Our findings indicate that the HA corona altered the bacterial toxicity mechanism of GNSs. Specifically, GNSs inflicted physical damage on the bacterial cell membrane, disrupting oxidative phosphorylation. This disruption led to the accumulation of ROS, inhibition of ATP synthesis, and ultimately bacterial death due to energy deficiency. In contrast, the HA corona on GNSs altered the electronic band structure, facilitating electron transfer that mediated the oxidation of biomolecules, where a certain level of physical membrane damage was crucial. This distinctive mechanism may also apply to other rod-shaped Gram-positive bacteria, such as *B. subtillis*. This discovery that HA attachment can enhance the bacterial toxicity of ENPs highlights the importance of understanding ecocorona activities to accurately evaluate the environmental risks of ENPs.

Methods

Materials and chemicals

Graphene nanosheets (GNSs) were purchased from XFNANO Materials Tech Co., Ltd. (Nanjing, China). *Bacillus tropicus* MCCC 1A01406 (*B. tropicus*) was provided by Heilongjiang Provincial Key Laboratory of Environmental Microbiology and Recycling of Argo-Waste in Cold Region (Daqing, China). *Escherichia coli* k12 (*E. coli* k12) was purchased from BeNa Culture Collection (Beijing, China). *Staphylococcus aureus* (*S. aureus*) was provided by Shenyang Institute of Applied Ecology, Chinese Academy of Sciences. *Bacillus subtilis* (*B. subtilis*) was provided by Molecule and Microbial Natural Product laboratory (Dr. Liwei Liu, Ningbo University). HCl and NaOH were purchased from Tianjin Kemio Chemical Reagent Co., Ltd. 2,7-Dichlorodihydrofluorescein

diacetate (DCFH-DA) was purchased from Beijing Puyihua Tech Co., Ltd. (Beijing, China). Hydrogen peroxide (H_2O_2) and ethyl alcohol were purchased from Tianjin Damao Chemical Reagent Factory. Ammonia was purchased from Shenyang Xinhua Reagent Factory. PBS buffer was purchased from Beijing Solarbio Science &Technology Co., Ltd. Melatonin and HEPES buffer were purchased from Shanghai Macklin Biochemical Co., Ltd. 1,2-Dioleoyl-sn-glycero-3-phosphocholine (DOPC) and Teflon (PTFE) were purchased from Sigma-Aldrich (USA). A Pt wire counter electrode and Ag/AgCl reference electrode were purchased from Wuhan Gaoshi Ruilian Technology Co., Ltd.

Humic acid (HA) was purchased from Sigma-Aldrich (USA) and underwent the following treatment before use. HA was dissolved in 0.01 M NaOH solution under ultrasonication, followed by adjusting the solution pH to 7.0 with 1.0 M HCl. The solution was centrifuged at 7000 *g* for 30 min, and then the supernatant was left standing overnight. HA was dialyzed through a dialysis membrane (1000 Da, Bluescape Scientific) to remove the chloride ions, and nitrate was used as a tracer agent to test chloride ions. The concentration of HA was quantified by UV absorbance at 254 nm (UV-2700, Shimadzu Corporation).

Adsorption of HA on GNSs

The batch equilibration technique was conducted to monitor the adsorption of HA on GNSs. A specific amount of GNSs was mixed with HA solution (pH=7) in a 20 mL glass vial sealed with Teflon-lined screw cap. For adsorption kinetics experiments, the final concentration of HA and GNSs in the mixture were 10 and 200 μg mL^{-1}, respectively. For the adsorption isotherm experiments, 1–50 μg mL^{-1} of HA and 200 μg mL^{-1} of GNSs were used. The solution pH was adjusted to 7.0 in all the groups and the vials were shaken at 150 rpm for 24 h to reach equilibrium. The mixture was centrifuged at 2200 *g* for 30 min, and then the concentration of HA in the supernatant was determined by UV absorbance at 254 nm. The precipitate obtained from the group of 50 mg mL^{-1} HA was defined as the complex of GNSs and HA (GNSs-HA), which was collected and stored in a sealed sample vial followed by lyophilization. All adsorption experiments were repeated at least three times and the results were reported as mean values.

The experimental data of adsorption kinetics were analyzed by fitting with quasi-first-order dynamics model (Eq. 5) and quasi-second-order dynamics model (Eq. 6).

$$Q_t = Q_e(1-e^{-K_1 t}) \tag{5}$$

$$Q_t = \frac{K_2 Q_e^{\ 2} t}{1+K_2 Q_e t} \tag{6}$$

Where Q_t (mg g^{-1}) and Q_e (mg g^{-1}) are the adsorption capacity of GNSs at t (min) and equilibrium time respectively; K_1 and K_2 (g mg^{-1} min^{-1}) are the rate constants of quasi-first order and quasi-second-order dynamics models, respectively.

The sorption isotherms were fitted to the Langmuir model (Eq. 7) and Freundlich model (Eq. 8).

$$Q_{max} = \frac{Q_m K_L C_e}{1+K_L C_e} \tag{7}$$

$$Q_{max} = K_F C_e^{\ 1/n} \tag{8}$$

Where Q_{max} (mg g^{-1}) is the theoretical maximum adsorption capacity, Q_m (mg g^{-1}) is the theoretical saturated adsorption capacity, C_e (μg mL^{-1}) is the remaining adsorbent in the solution, and K_L (L mg^{-1}) is the Langmuir model constant; K_F (L mg^{-1}) and n are the Freundlich model constants.

Characterizations

X-ray photoelectron spectroscopy (XPS) measurement was conducted on a ESCALAB250 (Thermo VG) with a monochromated Al Kα X-ray source. The infrared spectra were recorded by Fourier transform infrared spectroscopy (FTIR, Thermo Scientific) in the region of 400 – 4000 cm^{-1} with a resolution of 2 cm^{-1}. The morphology of GNSs and GNSs-HA were observed by scanning electron microscopy (SEM, S3400 II, Hitachi, Japan). The thickness and lateral size were characterized by atomic force electron microscopy (AFM, Agilent 5100, USA) in tapping mode in air. Raman spectra of GNSs and GNSs-HA were obtained by Raman spectroscopy (Thermo, Themol DXR, USA) with an excitation wavelength of 780 nm and scanning range from 60 to 1200 cm^{-1}.

Bacterial toxicity

HA (50 mg mL^{-1}) and GNSs (200 μg mL^{-1}) were mixed at pH 7.0 in a 20 mL glass vial sealed with a Teflon-lined screw cap. After shaking the vial at 150 rpm for 24 h, the mixture was centrifuged at 2200 *g* for 30 min to remove the supernatant. The resulting GNSs-HA was collected and washed three times with ultrapure water. Subsequently, it was rapidly frozen using liquid nitrogen and then dried in a freeze dryer. The dried GNSs-HA was transferred to a sealed sample vial for future use, and dispersed to the desired concentration using ultrapure water prior to experimental procedures. For the GNSs+HA group, GNSs and HA were directly mixed with bacterial suspension without pre-mixing. The bacterial toxicity of GNSs, GNSs-HA, and GNSs+HA was evaluated using optical density (OD) values and the colony counting method. Briefly, 1.0 mL of GNSs and GNSs-HA suspensions (0, 10, 100, 500, 1000, and 2000 μg mL^{-1}), 1.0 mL of bacterial suspension (10^5 CFU mL^{-1}), and 8.0 mL of fresh Luria Bertani (LB) broth were mixed together, obtaining the final material concentrations at 0, 1, 10, 50, 100, and 200 μg mL^{-1}. For the GNSs+HA group, 1.0 mL of bacterial suspension (10^5 CFU mL^{-1}), 1.0 mL of HA (14 μg mL^{-1}), 986 μg of GNSs powder, and 8.0 mL of fresh LB broth were mixed together. The quantity of GNSs (98.6 μg mL^{-1}) and HA (1.4 μg mL^{-1}) in GNSs+HA were identical to those in GNSs-HA at 100 μg mL^{-1} (Table S1). The mixtures were incubated at 37 °C and shaken at 150 rpm. The OD values were determined every 5 min at 600 nm on a microplate reader (BMG LABTECH, Germany) for 30 min to obtain the short-term growth curve. As a comparison, the effect of dissolved HA (1.4 μg mL^{-1}) on bacterial growth was evaluated following the same procedure. After 12 h incubation, the bacterial suspensions were diluted with sterilized water to a dilution series of 10^{-4}, 10^{-5}, and 10^{-6}. Then 100 μL of each dilution was spread onto a LB agar plate, which was incubated at 37 °C overnight. The colony forming units (CFUs) of all plates were counted and the survival rate (%) of *B. tropicus* was calculated by comparing the CFUs of treatment groups with that of controls.

Melatonin, as an antioxidant, was used to explore the role of ROS in the bacterial toxicity. Briefly, 0.5 mL of GNSs and GNSs-HA suspensions, 1.0 mL of *B. tropicus* suspension (10^5 CFU mL^{-1}), 8.0 mL of fresh LB broth, and 0.5 mL melatonin solution (20 μg mL^{-1}) were mixed together to obtain the final concentration of GNSs and GNSs-HA at 100 μg mL^{-1}. The mixtures were shaken at 120 rpm and incubated at 37 °C for 12 h. The survival rate of *B. tropicus* was evaluated using the colony counting method.

Oxidative stress

B. tropicus (10^9 CFU mL^{-1}) was co-cultured with GNSs and GNSs-HA (1, 10, 50, 100, 200 μg mL^{-1}) for 2 and 12 h at 37 °C. The bacterial cells were centrifuged at 10,509 g for 10 min, and then stained with 2,7-dichlorofluorescin-diacetate (DCFH-DA, 10 μM) for 30 min at 37 °C. After staining, the cells were collected by centrifugation at 10,509 g for 10 min, and then washed three times with PBS (pH=7.05) to remove excess dye. The fluorescence was visualized by confocal laser scanning

microscope (CLSM, TCS SP8 STED 3X, Leica, Germany) and quantified by a flow cytometer (BD FACSCalibur, USA).

Cell morphology

The morphologies of *B. tropicus* before and after treatment with GNSs or GNSs-HA were observed by SEM. After exposure to GNSs (50 and 100 μg mL^{-1}), GNSs-HA (50 and 100 μg mL^{-1}), GNSs+HA (GNSs: 98.6 μg mL^{-1}, HA: 1.4 μg mL^{-1}), and HA (1.4 μg mL^{-1}) for 12 h, the bacterial cells were centrifuged at 88 *g* for 5 min to remove most GNSs and GNSs-HA from the suspension. The bacterial cells were then collected by centrifugation at 10,509 *g* for 10 min, followed by washing three times with PBS. The bacterial cells were fixed with glutaraldehyde and gradually dehydrated with series concentrations of ethyl alcohol (50%, 70%, 90%, 100%) for 10 min, followed by lyophilization before visualization by SEM.

LDH assay

The release of lactate dehydrogenase (LDH) was quantified by a LDH cytotoxicity detection kit (Yuchun Bio-tech Inc., China). The bacterial suspension was treated with different concentrations of GNSs and GNSs-HA (0, 1, 10, 50, 100, 200 μg mL^{-1}) for 12 h at 37 °C. The mixtures were then centrifuged at 10509 *g* for 10 min, and the supernatant was mixed with the reagents according to the manufacturer instructions. The LDH release was measured by microplate reader at 450 nm.

Physical membrane damage

The interaction of GNSs and GNSs-HA with the model cell membrane was investigated by QCMD. Before the experiment, the gold-plated crystal sensor was cleaned by immersion in a mixed solution (H_2O: 30% H_2O_2: 25% NH_3 = 5:1:1) for 5 min at 75 °C, and then rinsed with a large amount of deionized water before drying under nitrogen. The sensor was then oxidized by UV ozone exposure for 20 min, followed by rinsing with Millipore water and drying with nitrogen gas.

To prepare the model membrane, chloroform solution of 1,2-dioleoyl-sn-glycero-3-phosphocholine (DOPC, 25 mg mL^{-1}, 0.2 mL) was added into a conical flask and dried under nitrogen to form a DOPC film, which was vacuum dried for more than 4 h to remove residual chloroform. Then 5 mL HEPES buffer solution was added under continuous magnetic stirring for 30 min to form DOPC vesicles. The DOPC solution was passed through a polycarbonate film (Whatman) back and forth for more than 15 times by a micro lipid extruder (Avanti Polar Lipids Inc.). A single layer of vesicles with a hydrodynamic diameter of 192–194 nm was obtained. The vesicle suspension was sealed with nitrogen in a glass bottle at 4 °C and used within 4 days after preparation.

During the QCMD test, the temperature in the flow cell chamber was kept at 37 °C, and the liquid flow rate was 150 μL min^{-1}. The frequency (representing the deposited mass) and energy dissipation (representing the viscoelastic properties of the deposited layer) were detected. HEPES buffer was first introduced to the system until the signal was stable. Afterwards, DOPC vesicles were introduced to form a supporting vesicle layer on the sensor surface. Then HEPES buffer was injected again to remove the unadsorbed DOPC vesicles. GNSs and GNSs-HA were then suspended in HEPES (50 and 100 μg mL^{-1}) to initiate the interaction process, followed by rinsing with HEPES to remove the unadsorbed GNSs and GNSs-HA. At the end of each experiment, 1% Triton X-100 (a membrane solubilizer) was used to remove the adsorbed vesicles.

Electrochemical measurement

GNSs or GNSs-HA powders were mixed with a polytetrafluoroethylene solution (2 wt%), and the mixture was pasted on the surface of carbon fiber paper (surface area of 2.5 cm^2) with a loading content of 0.5 mg cm^{-2}. After drying at 100 °C for 3 h in the oven, the final electrode material was obtained. A bacterial suspension (100 mL) with an initial concentration of 10^5 CFU mL^{-1} was incubated at 37 °C for 12 h before use. *B. tropicus* cells were harvested by centrifugation at 10509 *g* for 3 min and washed three times with anaerobic PBS (0.1 M, pH 7.0). The *B. tropicus* cells were resuspended in PBS and diluted to ~10^9 CFU mL^{-1}. The bacterial suspension was deoxygenated by purging with nitrogen for 30 min before each test. In the GNSs+HA treatment group, GNSs were used as electrodes and HA (1.4 μg mL^{-1}) was added to the bacterial suspension. Electrochemical measurements were conducted by an electrochemical workstation (CHI660E, CH Instruments, Inc., Shanghai, China). A three-electrode cell was setup, consisting of a GNSs- or GNSs-HA-loaded carbon fiber paper working electrode, a Pt wire counter electrode, and an Ag/AgCl reference electrode. CV measurements were carried out at a scan rate of 100 mV s^{-1} and over a potential range from −0.6 to 0.1 V for GNSs, from −0.9 to 0.1 V for GNSs-HA, and from −0.35 to 0.1 V for GNSs+HA. Electrochemical impedance spectra (EIS) were obtained over frequencies ranging from 1000 kHz to 1 Hz, with an amplitude of 5 mV. LSV was obtained at a scan rate of 50 mV s^{-1}.

Local surface potential measurement by KPFM

After *B. tropicus* were incubated with GNSs (50 and 100 μg mL^{-1}), GNSs-HA (50 and 100 μg mL^{-1}), GNSs+HA (GNSs: 98.6 μg mL^{-1}, HA: 1.4 μg mL^{-1}), and HA (1.4 μg mL^{-1}) for 60 min at 37 °C, the mixture was centrifuged at 88 *g* for 5 min to remove the agglomerates, followed by dropping the suspension onto a monocrystalline silicon wafer. As soon as the sample was dried under ambient conditions, the silicon wafer with fixed samples was finally adhered to a small piece (1 cm × 1 cm) of conductive double-sided tape, which was placed on a grounded microscope stage for KPFM measurement. Three bacterial cells were analyzed for each sample in order to verify that the microscopy images represented the average potential of the samples. KPFM was conducted in the tapping mode on the Agilent 5500 AFM. Platinum (Pt)/iridium (Ir)-coated silicon cantilever probes (Bruker, SCM-PIT-V2) were used as the conductive probes with a force constant of approximately 3 N m^{-1} and a nominal resonance frequency of 75 kHz.

MDA content

The content of malondialdehyde (MDA) was quantified using a commercial kit (Nanjing Jiancheng, China). After treatment with GNSs and GNSs-HA (1, 10, 50, 100, 200 μg mL^{-1}) for 12 h at 37 °C, the bacterial cells were harvested and disrupted by an ultrasonic processor. After centrifugation, thiobarbituric acid (TBA) was added and the mixture was incubated for 40 min at 95 °C, and then cooled to room temperature. The absorbance of supernatant at 532 nm was determined by a microplate reader.

GSH/GSSG ratio

The concentrations of glutathione (GSH) and glutathione disulfide (GSSG) were measured by a commercial kit (Beyotime Biotechnology, China). After treatment with GNSs and GNSs-HA (1, 10, 50, 100, 200 μg mL^{-1}) for 12 h at 37 °C, the bacterial cells were harvested by centrifugation, followed by washing with PBS. After adding the protein removal reagent (40 μL), the samples were rapidly frozen with liquid nitrogen, thawed in water bath at 37 °C, crushed with grinding pestle, and placed in ice bath for 5 min. The supernatants were acquired by centrifugation for 5 min at 10509 *g*. The contents of GSH and GSSG were determined according to the manufacturer instructions and the absorbance at 412 nm was measured by microplate reader to calculate the ratio of GSH to GSSG (GSH/GSSG).

ATP content

The content of adenosine triphosphate (ATP) was quantified using a commercial kit (Biosharp, China). After treatment with GNSs and GNSs-HA at the concentrations of 50 and 100 μg mL^{-1} for 12 h at 37 °C, the bacterial cells were mixed with an ATP extracting solution, and

then disrupted by an ultrasonic processor. The supernatants were harvested by centrifugation for 5 min at 10,509 g, placed on ice before testing, and mixed with the reagents following the manufacturer instructions.

Oxygen consumption analysis

To measure the oxygen consumption rate, 100 mL of bacterial suspension with an initial concentration of 10^5 CFU mL^{-1} was cultured for 12 h before use. The cells were then harvested by centrifugation (10509 *g* at 4 °C for 10 min), washed twice with PBS, and resuspended in 100 mL PBS (pH 7.0). GNSs and GNSs-HA (2000 μg mL^{-1}, 0.5 mL) were added to the bacterial suspension (9.5 mL) to obtain a final concentration at 100 μg mL^{-1} and were then co-cultured for 30 min at 37 °C. The real time oxygen content was then measured every 5 min by portable dissolved oxygen analyzer (OHAUS STARTER 400D), and the oxygen consumption rate (%) was represented as follows:

$$\text{Oxygen consumptio n rate} = \frac{\text{Dissolved oxygen concentrat ion}\,(t+5) - \text{Dissolved oxygen concentrat ion}\,(t)}{\text{OD} \times 5} \quad (t = 5, 10, 15, 20, 25 min) \tag{9}$$

Extracellular ROS level

A volume of 100 mL of bacterial suspension (initial concentration of 10^5 CFU mL^{-1}) was incubated for 12 h. The bacterial cells were harvested by centrifugation (10509 g at 4 °C for 10 min), washed twice, and resuspended in 100 mL PBS buffer (PH 7.0). GNSs and GNSs-HA suspensions (2000 μg mL^{-1}, 0.5 mL) were added to the bacterial suspension (9.5 mL) in the presence or absence of melatonin (1 μg mL^{-1}). The following control groups were prepared: PBS (10 mL), bacterial suspension (9.5 mL) + PBS (0.5 mL), PBS (9.5 mL) + GNSs (0.5 mL), PBS (9.5 mL) + GNSs-HA (0.5 mL), bacterial suspension (9.5 mL) + H_2O_2 (1%, 0.5 mL). All groups were incubated for 30 min at 37 °C and then centrifuged at 10,509 *g* for 10 min. DCFH-DA (10 μM) was added to the supernatants and the mixtures were incubated for 30 min at 37 °C. The fluorescence intensity was then quantified by using a microplate reader.

DNA oxidation

The degree of DNA oxidation was evaluated by measuring the content of 8-hydroxy-desoxyguanosine (8-OHdG) using a commercial kit (Beyotime Biotechnology). After treatment with GNSs and GNSs-HA (100 μg mL^{-1}) for 12 h at 37 °C, the bacterial cells were harvested, washed with PBS once, and resuspended in PBS. The OD_{600} values of all bacterial suspensions were adjusted to 0.3 by microplate reader. The samples were prepared according to kit instructions, and the absorbance was measured at 450 nm by microplate reader.

Proteomics and transcriptomics

Bacterial cells were incubated with GNSs (50 and 100 μg mL^{-1}), GNSs-HA (50 and 100 μg mL^{-1}), GNSs+HA (GNSs: 98.6 μg mL^{-1}, HA: 1.4 μg mL^{-1}), and HA (1.4 μg mL^{-1}) for 60 min, and the mixtures were centrifuged at 88 g for 5 min to remove the agglomerated materials. The suspension was then centrifuged at 10,509 *g* for 10 min to collect the bacterial cells, which were rinsed by PBS three times before transfer to an RNase and DNase free centrifuge tube. The samples were sent to Shanghai Personal Biotechnology Co., Ltd. for prokaryotic transcriptome sequencing and proteomic analysis using Illumina MiSeq sequencing platform or Liquid Chromatography Coupled to Tandem Mass Spectrometry (LC-MS/MS) analysis, respectively (Thermo Scientific). FPKM (fragments per kilobases per million fragments) was used to standardize the levels of gene expression, so as to calculate the transcript abundance. The differentially expression genes (DEGs) were identified by the following standard: the expression difference multiple |log2 Fold Change| > 1 and $P < 0.05$. All DEGs were mapped to the Kyoto Encyclopedia of Genes and Genomes database (KEGG) and Gene Ontology database (GO). After sequencing, all raw reads were uploaded to the NCBI Sequence Read Archive (SRA, https://submit.ncbi.nlm.nih.gov/subs/sra/) database (Accession number: PRJNA977448). The differentially abundant proteins (DAPs) were identified with the following standard: the expression difference multiple |log2 Fold Change| > 2 and $P < 0.05$. All DAPs were mapped to KEGG and GO.

Band structure calculation

The valence band and band gap of HA and GNSs-HA were determined by XPS and UV diffuse reflectance spectroscopy. In the UV diffuse reflectance spectrum, the extension of the straight line on the right intersects with the extension of the horizontal line, and the abscissa of the intersection point is the material valence band. The band gap diagram was drawn with $(\alpha h\nu)^2$ as the y-axis and hv as the x-axis ($h\nu = hc/\lambda$, c: lightspeed, λ: wavelength of light). The straight line portion in the curve was extrapolated to the x-axis (y = 0), and the intersection point correspond to the band gap value.

Statistics and reproducibility

No data were excluded from the analyses. The investigators were blinded to allocation during experiments and outcome assessment.

Reporting summary

Further information on research design is available in the Nature Portfolio Reporting Summary linked to this article.

Data availability

The transcriptomic data generated in this article have been deposited in the NCBI Sequence Read Archive database under accession code PRJNA977448. The proteomic data generated in this article has been deposited in the proteome xchange submission tool under accession code PXD043749 and PXD056079. All other relevant data generated and analysed during this study are included in the manuscript and supplementary information. Source data is available for Figs. 1a–h, 2a, 2c–h, and 3d–g and Supplementary Figs. 1, 4, 5a–c, 6a, b, 7, 9d, e, 10, 14, 15, 16, 17, 18, 19, 20, 22, 23, 24, 26, 27d–i, 28, 30, and 31a–c in the associated source data file. Source data are provided with this paper.

References

1. Novoselov, K. et al. Electric Field Effect in Atomically Thin Carbon Films. *Science* **306**, 666–669 (2004).
2. Khan, K. et al. Recent developments in emerging two-dimensional materials and their applications. *J. Mater. Chem. C* **8**, 387–440 (2020).
3. Zou, W., Zhou, Q., Zhang, X. & Hu, X. Environmental Transformations and Algal Toxicity of Single-Layer Molybdenum Disulfide Regulated by Humic Acid. *Environ. Sci. & Technol.* **52**, 2638–2648 (2018).
4. Zhao, J. et al. Humic acid mitigated toxicity of graphene-family materials to algae through reducing oxidative stress and heteroaggregation. *Enviro. Sci.: Nano* **6**, 1909–1920 (2019).

5. Su, Y. et al. Green Algae as Carriers Enhance the Bioavailability of (14)C-Labeled Few-Layer Graphene to Freshwater Snails. *Environ. Sci. Technol.* **52**, 1591–1601 (2018).
6. Chen, W. et al. Black Phosphorus Nanosheets as a Neuroprotective Nanomedicine for Neurodegenerative Disorder Therapy. *Adv. Mater.* **30**, 1703458 (2018).
7. Jannesari, M., Akhavan, O., Madaah Hosseini, H. R. & Bakhshi, B. Graphene/CuO(2) Nanoshuttles with Controllable Release of Oxygen Nanobubbles Promoting Interruption of Bacterial Respiration. *ACS Appl. Mater. Interfaces* **12**, 35813–35825 (2020).
8. Zhou, H. et al. The inhibition of migration and invasion of cancer cells by graphene via the impairment of mitochondrial respiration. *Biomaterials* **35**, 1597–1607 (2014).
9. Xu, L. et al. The Crucial Role of Environmental Coronas in Determining the Biological Effects of Engineered Nanomaterials. *Small* **16**, e2003691 (2020).
10. Li, J. et al. Temperature-responsive tungsten doped vanadium dioxide thin film starves bacteria to death. *Mater. Today* **22**, 35–49 (2019).
11. He, X. et al. Assessing the effects of surface-bound humic acid on the phototoxicity of anatase and rutile TiO(2) nanoparticles in vitro. *J. Environ. Sci. (China)* **42**, 50–60 (2016).
12. Mao, H. Y. et al. Manipulating the electronic and chemical properties of graphene via molecular functionalization. *Prog. Surf. Sci.* **88**, 132–159 (2013).
13. Cai, W. et al. Natural antioxidant functionalization for fabricating ambient-stable black phosphorus nanosheets toward enhancing flame retardancy and toxic gases suppression of polyurethane. *J. Hazard. Mater.* **387**, 121971 (2020).
14. Peng, H., Wang, D. & Fu, S. Tannic acid-assisted green exfoliation and functionalization of MoS2 nanosheets: Significantly improve the mechanical and flame-retardant properties of polyacrylonitrile composite fibers. *Chem. Eng. J.* **384**, 123288 (2020).
15. Deng, C.-H. et al. Graphene–CdS nanocomposite inactivation performance toward Escherichia coli in the presence of humic acid under visible light irradiation. *Chem. Eng. J.* **284**, 41–53 (2016).
16. Das, N. M., Singh, A. K., Ghosh, D. & Bandyopadhyay, D. Graphene oxide nanohybrids for electron transfer-mediated antimicrobial activity. *Nanoscale Adv* **1**, 3727–3740 (2019).
17. Shang, E. et al. Relative importance of humic and fulvic acid on ROS generation, dissolution, and toxicity of sulfide nanoparticles. *Water Res* **124**, 595–604 (2017).
18. Zhang, X., Sui, M., Yan, X., Huang, T. & Yuan, Z. Mitigation in the toxicity of graphene oxide nanosheets towards Escherichia coli in the presence of humic acid. *Environ. Sci.: Process Impacts* **18**, 744–750 (2016).
19. Zhang, Y. et al. The effects of humic acid on the toxicity of graphene oxide to Scenedesmus obliquus and Daphnia magna. *Sci. Total Environ.* **649**, 163–171 (2019).
20. Hong, Y., Zeng, J., Wang, X., Drlica, K. & Zhao, X. Post-stress bacterial cell death mediated by reactive oxygen species. *Proc. Natl. Acad. Sci. USA* **116**, 10064–10071 (2019).
21. Liu, S. et al. Antibacterial Activity of Graphite, Graphite Oxide, Graphene Oxide, and Reduced Graphene Oxide: Membrane and Oxidative Stress. *ACS Nano* **5**, 6971–6980 (2011).
22. Oktyabrsky, G. V. S. O. N. Glutathione in Bacteria. *Biochemistry (Moscow)* **70**, 1199 (2005).
23. Yang, S. P. et al. Influence of humic acid on titanium dioxide nanoparticle toxicity to developing zebrafish. *Environ. Sci. Technol.* **47**, 4718–4725 (2013).
24. Feng, Y. et al. Interaction of Graphitic Carbon Nitride with Cell Membranes: Probing Phospholipid Extraction and Lipid Bilayer Destruction. *Environ. Sci. Technol.* **56**, 17663–17673 (2022).
25. Hu, X., Ouyang, S., Mu, L., An, J. & Zhou, Q. Effects of Graphene Oxide and Oxidized Carbon Nanotubes on the Cellular Division, Microstructure, Uptake, Oxidative Stress, and Metabolic Profiles. *Environ. Sci. Technol.* **49**, 10825–10833 (2015).
26. Zhou, Q. & Hu, X. Systemic Stress and Recovery Patterns of Rice Roots in Response to Graphene Oxide Nanosheets. *Environ. Sci. Technol.* **51**, 2022–2030 (2017).
27. Gerbino, E., Carasi, P., Mobili, P., Serradell, M. A. & Gomez-Zavaglia, A. Role of S-layer proteins in bacteria. *World J. Microbiol. Biotechnol.* **31**, 1877–1887 (2015).
28. Meyer, T. E. & Cusanovich, M. A. Discovery and characterization of electron transfer proteins in the photosynthetic bacteria. *Photosynth. Res.* **76**, 111–126 (2003).
29. Haddock, B. A. & Jones, C. W. Bacterial respiration. *Bacteriol. Rev.* **41**, 47–99 (1977).
30. Llorente-Garcia, I. et al. Single-molecule in vivo imaging of bacterial respiratory complexes indicates delocalized oxidative phosphorylation. *Biochim. Biophys. Acta* **1837**, 811–824 (2014).
31. Trounce, I. Genetic control of oxidative phosphorylation and experimental models of defects. *Hum. Reprod.* **15**, 18–27 (2000).
32. Leif, H., Sled, V. D., Ohnishi, T., Weiss, H. & Friedrich, T. Isolation and Characterization of the Proton-translocating NADH:ubiquinone Oxidoreductase from Escherichia coli. *Eur. J. Biochem.* **230**, 538–548 (1995).
33. Friedrich, T. et al. Redox components and structure of the respiratory NADH:ubiquinone oxidoreductase (complex I). *BBA-Bioenergetics* **1365**, 215–219 (1998).
34. Sabharwal, S. S. & Schumacker, P. T. Mitochondrial ROS in cancer: initiators, amplifiers or an Achilles' heel? *Nat. Rev. Cancer* **14**, 709–721 (2014).
35. Elston, T., Wang, H. & Oster, G. Energy transduction in ATP synthase. *Nature* **391**, 510–513 (1998).
36. Cui, Y. et al. The molecular mechanism of action of bactericidal gold nanoparticles on Escherichia coli. *Biomaterials* **33**, 2327–2333 (2012).
37. Cui, Y. & Qu, X. Genetic mechanisms of prebiotic carbohydrate metabolism in lactic acid bacteria: Emphasis on Lacticaseibacillus casei and Lacticaseibacillus paracasei as flexible, diverse and outstanding prebiotic carbohydrate starters. *Trends Food Sci. & Tech.* **115**, 486–499 (2021).
38. Komosinska-Vassev, K. et al. Alterations of glycosaminoglycan metabolism in the development of diabetic complications in relation to metabolic control. *Clin. Chem. Lab. Med.* **43**, 924–929 (2005).
39. Sobhanifar, S., King, D. T. & Strynadka, N. C. J. Fortifying the wall: synthesis, regulation and degradation of bacterial peptidoglycan. *Curr. Opin. Struc. Biol.* **23**, 695–703 (2013).
40. Kaila, V. R. I. & Wikstrom, M. Architecture of bacterial respiratory chains. *Nat. Rev. Microbiol.* **19**, 319–330 (2021).
41. Tan, J. et al. A facile and universal strategy to endow implant materials with antibacterial ability via alkalinity disturbing bacterial respiration. *Biomater. Sci.* **8**, 1815–1829 (2020).
42. Chen, S. et al. MoS2 Nanosheets-Cyanobacteria Interaction: Reprogrammed Carbon and Nitrogen Metabolism. *ACS Nano* **15**, 16344–16356 (2021).
43. Li, J. et al. Antibacterial activity of large-area monolayer graphene film manipulated by charge transfer. *Sci. Rep.* **4**, 4359 (2014).
44. Zhou, S., Lin, M., Zhuang, Z., Liu, P. & Chen, Z. Biosynthetic graphene enhanced extracellular electron transfer for high performance anode in microbial fuel cell. *Chemosphere* **232**, 396–402 (2019).
45. Huang, B. et al. Ferroferric oxide loads humic acid doped anode accelerate electron transfer process in anodic chamber of bioelectrochemical system. *J. Electroanal. Chem.* **851**, 113464 (2019).
46. Li, J. et al. Band Gap Engineering of Titania Film through Cobalt Regulation for Oxidative Damage of Bacterial Respiration and Viability. *ACS Appl. Mater. Interfaces* **9**, 27475–27490 (2017).

47. Qu, G. et al. Property-Activity Relationship of Black Phosphorus at the Nano-Bio Interface: From Molecules to Organisms. *Chem. Rev.* **120**, 2288–2346 (2020).
48. Deokar, A. R., Lin, L. Y., Chang, C. C. & Ling, Y. C. Single-walled carbon nanotube coated antibacterial paper: preparation and mechanistic study. *J. Mater. Chem. B* **1**, 2639–2646 (2013).
49. Pulingam, T. et al. Graphene oxide exhibits differential mechanistic action towards Gram-positive and Gram-negative bacteria. *Colloids Surf. B Biointerfaces* **181**, 6–15 (2019).
50. Wang, M. et al. Interaction with teichoic acids contributes to highly effective antibacterial activity of graphene oxide on Gram-positive bacteria. *J. Hazard. Mater.* **412**, 125333 (2021).
51. Xiong, Z. et al. Transcriptome Analysis Reveals the Growth Promotion Mechanism of Enteropathogenic Escherichia coli Induced by Black Phosphorus Nanosheets. *ACS Nano* **17**, 3574–3586 (2023).
52. Xiong, Z. et al. Bacterial toxicity of exfoliated black phosphorus nanosheets. *Ecotoxicol. Environ. Saf.* **161**, 507–514 (2018).
53. Ghaderi, O. A. E. Toxicity of Graphene and Graphene Oxide Nanowalls Against Bacteria. *ACS Nano* **4**, 5731–5736 (2010).
54. Yang, L. Electrical impedance spectroscopy for detection of bacterial cells in suspensions using interdigitated microelectrodes. *Talanta* **74**, 1621–1629 (2008).
55. Pham, V. T. et al. Ivanova Graphene Induces Formation of Pores That Kill Spherical and Rod-Shaped Bacteria. *ACS Nano* **9**, 8458–8467 (2015).

Acknowledgements

This work was supported by the National Natural Science Foundation of China (No. 42192574 to Q.Z., 42394150 to F.W., 42277423 to X.Z., 42077394 to X.Z., 42230713 to F.W., 42377417 to Q.Z.), Guangdong Major Project of Basic and Applied Basic Research (2023B0303000006 to F.W.), National Key Research and Development Program of China (2023YFC3708700 to X.Z.), GDAS' Project of Science and Technology Development (2022GDASZH-2022010105 to X.Z., 2023GDASQNRC-0103 to Q.Z., 2023GDASQNRC-0106 to X.Z., and 2020GDASYL-20200101002 to F.W.), and Guangdong Foundation for Program of Science and Technology Research (Grant No.2023B1212060044 to F.L.).

Author contributions

X.Z. conceived the idea and designed the research. J. Z. performed most of the experiments. Z.X., S.Z., and J.Y. analyzed the omics data. W.T., and Y.X. interpreted the data. X.Z. and Q.Z. contributed to writing the manuscript. J.C.W., F.L., B.X. and F.W. modified the manuscript.

Competing interests

The authors declare no competing interests.

Additional information

Supplementary information The online version contains supplementary material available at https://doi.org/10.1038/s41467-024-55270-2.

Correspondence and requests for materials should be addressed to Qing Zhao, Fengchang Wu or Baoshan Xing.

Peer review information *Nature Communications* thanks the anonymous reviewers for their contribution to the peer review of this work. A peer review file is available.